JACS
JOURNAL OF THE AMERICAN CHEMICAL SOCIETY
Article
pubs.acs.org/JACS

Mixed-Metal Carbonate Fluorides as Deep-Ultraviolet Nonlinear Optical Materials

T. Thao Tran,[†,§] Joshua Young,[‡,∥] James M. Rondinelli,*[,‡] and P. Shiv Halasyamani*[,†]

[†]Department of Chemistry, University of Houston, 112 Fleming Building, Houston, Texas 77204-5003, United States
[‡]Department of Materials Science and Engineering, Northwestern University, 2220 Campus Drive, Evanston, Illinois 60208-3108, United States

Supporting Information

ABSTRACT: Noncentrosymmetric mixed-metal carbonate fluorides are promising materials for deep-ultraviolet (DUV) nonlinear optical (NLO) applications. We report on the synthesis, characterization, structure−property relationships, and electronic structure calculations on two new DUV NLO materials: $KMgCO_3F$ and $Cs_9Mg_6(CO_3)_8F_5$. Both materials are noncentrosymmetric (NCS). $KMgCO_3F$ crystallizes in the achiral and nonpolar NCS space group $P\bar{6}2m$, whereas $Cs_9Mg_6(CO_3)_8F_5$ is found in the polar space group $Pmn2_1$. The compounds have three-dimensional structures built up from corner-shared magnesium oxyfluoride and magnesium oxide octahedra. $KMgCO_3F$ ($Cs_9Mg_6(CO_3)_8F_5$) exhibits second-order harmonic generation (SHG) at both 1064 and 532 nm incident radiation with efficiencies of 120 (20) × α-SiO_2 and 0.33 (0.10) × β-BaB_2O_4, respectively. In addition, short absorption edges of <200 and 208 nm for $KMgCO_3F$ and $Cs_9Mg_6(CO_3)_8F_5$, respectively, are observed. We compute the electron localization function and density of states of these two compounds using first-principles density functional theory, and show that the different NLO responses arise from differences in the denticity and alignment of the anionic carbonate units. Finally, an examination of the known SHG active $AMCO_3F$ (A = alkali metal, M = alkaline earth metal, Zn, Cd, or Pb) materials indicates that, on average, smaller A cations and larger M cations result in increased SHG efficiencies.

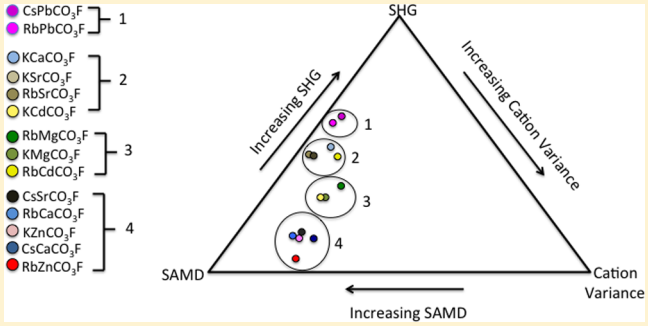

INTRODUCTION

Coherent deep-ultraviolet (DUV) light, λ < 200 nm, has a variety of technologically important uses, including photolithography, attosecond pulse generation, and in advanced instrument development.[1−4] One manner in which to generate coherent DUV light is through cascaded frequency conversion using nonlinear optical (NLO) materials—specifically the sixth harmonic generation of Nd:YAG (1064 nm) radiation—177.3 nm. As such, NLO materials capable of generating coherent DUV light are of considerable interest.[5−14] For a material to have DUV NLO applications, the following attributes are necessary: (i) crystallographic noncentrosymmetric (NCS) structure, (ii) large transparency window, i.e. wide band gap, (iii) large second-harmonic generating (SHG) coefficients, (iv) moderate birefringence, (v) chemical stability with a large damage threshold, and (vi) easy growth of large (cm^3) single crystals. At present, only $KBe_2BO_3F_2$ is capable of generating coherent light in the DUV;[15] however, single crystals of $KBe_2BO_3F_2$ are layered along their optic axis, preventing large crystals from being grown.[15−17] Also, the need for highly toxic BeO in the synthesis and crystal growth has limited the broad technological use of $KBe_2BO_3F_2$.

Besides $KBe_2BO_3F_2$, other NLO borate crystals have been used in photonic applications, e.g., LiB_3O_5,[18] CsB_3O_5,[19,20] and β-BaB_2O_4 (β-BBO).[21] The absorption edges of LiB_3O_5 and CsB_3O_5 are well below 200 nm, 155 and 167 nm, respectively;[18−20] however their relatively poor birefringence (0.045) (LiB_3O_5) and 0.063 (CsB_3O_5) precludes their use for DUV NLO applications. A larger birefringence of 0.1127 is observed in β-BBO,[21] which results in a large walk-off angle, reducing its SHG efficiency. Also, the absorption edge of β-BBO is 185 nm.[20] Thus, sixth-harmonic Nd:YAG generation is not possible.

A number of other design strategies toward the creation of new NLO materials have been reported. These involve using distorted chalcogenide polyhedra,[22−24] cations susceptible to second-order Jahn−Teller distortions,[25−28] and cations with a stereoactive lone-pair of electrons.[29−36] An issue with these design approaches is that either the birefringence is not appropriate or the absorption edge is not deep enough for DUV NLO applications.

A family of materials that has promising DUV NLO applications is mixed-metal carbonate fluorides.[37,38] Specifically, mixed-metal carbonates exhibit: (i) fully bonded $(CO_3)^{2-}$ groups, i.e. there is (are) no terminal oxygen atom(s) (in

Received: November 19, 2016
Published: December 24, 2016

DOI: 10.1021/jacs.6b11965
J. Am. Chem. Soc. 2017, 139, 1285−1295

borates, it has been demonstrated that dangling or terminal oxygen atoms(s) red-shift the absorption edge[39−41]), and (ii) a blue-shift of the absorption edge attributable to the inclusion of fluoride. Mixed-metal carbonate fluorides are synthetically accessible through both hydrothermal methods for crystal growth and ceramic reactions for bulk powder. A few NCS carbonate fluorides have been reported, including $Na_8Lu_2(CO_3)_6F_2$,[42] $Na_8Lu(CO_3)_2F_2$,[42] A-Pb-CO_3-F (A = K, Rb, or Cs),[43−45] A-B-CO_3-F (A = K, Rb, or Cs; B = Ca, Sr, or Ba),[46,47] and $KCdCO_3F$,[48−50] $RbCdCO_3F$,[49,50] and $AZnCO_3F$ (A = K or Rb).[50] Recently, we reported a new DUV NLO compound: $RbMgCO_3F$.[51] The material is SHG active at both 1064 and 532 nm, and it exhibits a UV absorption edge at 190 nm. Electronic structure calculations suggested that the nonuniform ligand bonding of Mg^{2+}—mono- and bidentate—enhances the SHG response of $RbMgCO_3F$. Additional investigation of the alkali-metal magnesium carbonate fluorides resulted in the discovery of two new NLO materials: $KMgCO_3F$ and $Cs_9Mg_6(CO_3)_8F_5$. In this paper, we report the synthesis, crystal structure, characterization, and functional properties of $KMgCO_3F$ and $Cs_9Mg_6(CO_3)_8F_5$. In addition, atomic scale analyses were performed to better describe the underlying origin of the acentric properties of these materials as well as other known NLO active carbonate fluorides.

EXPERIMENTAL SECTION

Reagents. Potassium fluoride, cesium fluoride (Alfa Aesar, 99.5%), and magnesium carbonate basic (Sigma-Aldrich, ≥40% Mg basis as MgO) were used as starting materials.

Synthesis. Polycrystalline $KMgCO_3F$ and $Cs_9Mg_6(CO_3)_8F_5$ were synthesized through conventional solid-state techniques. $MgCO_3$ was pretreated by heating magnesium carbonate basic to 270 °C for 15 h in CO_2 flowing gas. KF and CsF were dried at 110 °C for 10 h before use. For $KMgCO_3F$, stoichiometric amounts of KF (0.232 g, 4.00×10^{-3} mol) and $MgCO_3$ (0.337 g, 4.00×10^{-3} mol) were thoroughly ground and pressed into a pellet. The pellet was placed in an alumina boat that was heated to 330 °C in flowing CO_2 gas and held for 7 days, with intermittent regrindings, and then cooled to room temperature at a rate of 180 °C h^{-1}. For $Cs_9Mg_6(CO_3)_8F_5$, stoichiometric amounts of CsF (0.760 g, 5.00×10^{-3} mol), Cs_2CO_3 (0.652 g, 2.00×10^{-3} mol), and $MgCO_3$ (0.506 g, 6.00×10^{-3} mol) were thoroughly ground and pressed into a pellet. The pellet was placed in an alumina boat that was heated to 345 °C in flowing CO_2 gas and held for 10 days, with intermittent regrindings, and then cooled to room temperature at a rate of 180 °C h^{-1}.

Crystals of $KMgCO_3F$ and $Cs_9Mg_6(CO_3)_8F_5$ were grown by solvothermal techniques. For $KMgCO_3F$, the reaction mixture of 0.017 g (0.30×10^{-3} mol) of KF, 0.426 g (3.00×10^{-3} mol) of polycrystalline $KMgCO_3F$, and 2.00 mL (0.11×10^{-3} mol) of water was placed in a 23 mL Teflon-lined stainless steel autoclave. The autoclave was closed, gradually heated up to 230 °C, held for 9 days, and then slowly cooled to room temperature at a rate of 6 °C h^{-1}. The solid products were isolated from the mother-liquor by vacuum filtration and washed with ethanol. Under similar conditions, crystals of $Cs_9Mg_6(CO_3)_8F_5$ were grown by combining 0.030 g (0.20×10^{-3} mol) of CsF, 1.917 g (1.00×10^{-3} mol) of polycrystalline $Cs_9Mg_6(CO_3)_8F_5$, 0.033 g (0.10×10^{-3} mol) of Cs_2CO_3, and 3.00 mL (0.16×10^{-3} mol) of water. The autoclave was closed, gradually heated up to 230 °C, held for 14 days, and then slowly cooled to room temperature at a rate of 6 °C h^{-1}. Colorless hexagonal-prism-shaped and block-shaped crystals, subsequently determined to be $KMgCO_3F$ and $Cs_9Mg_6(CO_3)_8F_5$, were obtained in approximately 70% and 60% yields, respectively, based on polycrystalline $KMgCO_3F$ and $Cs_9Mg_6(CO_3)_8F_5$. The materials were determined to be pure by powder X-ray diffraction (Figure S1).

Single-crystal X-ray diffraction. A colorless hexagonal prism crystal ($0.09 \times 0.08 \times 0.07$ mm^3) and a colorless block-shaped crystal ($0.20 \times 0.14 \times 0.06$ mm^3) were selected for single-crystal diffraction analysis. Data were collected on a Bruker platform diffractometer equipped with a 4K CCD APEX II detector using graphite-monochromated Mo Kα radiation. For each sample, a hemisphere of data (3061 frames at 6 cm detector distance) was collected using a narrow-frame algorithm with scan widths of 0.30° in omega and an exposure time of 60 s per frame. Data were integrated using the Bruker SAINT program,[52] with the intensities corrected for the Lorentz factor, polarization, air absorption, and absorption attributable to the variation in the path length through the detector faceplate. An empirical absorption correction was applied based on the entire data set. Redundant reflections were averaged. The positions of the potassium (or cesium) and magnesium atoms were determined by direct methods using SHELXS-97,[53] and the remaining atoms were located by difference Fourier maps and least-squares cycles utilizing SHELXL-97.[54] All calculations were performed using the WinGX-98 crystallographic software package.[55] Relevant crystallographic data for $KMgCO_3F$ and $Cs_9Mg_6(CO_3)_8F_5$ are given in Table 1. Selected bond distances and angles, atomic coordinates, and equivalent isotropic displacement parameters have been deposited in the Supporting Information (Tables S1−S3).

Table 1. Crystallographic Data

	$KMgCO_3F$	$Cs_9Mg_6(CO_3)_8F_5$
M/g mol^{-1}	142.42	1917.13
T/K	293(2)	296(2)
λ/Å	0.71073	0.71073
Crystal system	Hexagonal	Orthorhombic
Space group	$P\bar{6}2m$ (No. 189)	$Pmn2_1$ (No. 31)
a/Å	8.8437(2)	13.2888(17)
b/Å	8.8437(2)	6.8258(9)
c/Å	3.9254(1)	18.824(2)
V/Å^3	265.88(2)	1707.4(4)
Z	3	2
d_c/g cm^{-3}	2.668	3.729
μ/mm^{-1}	1.550	9.715
$2\theta_{max}$/deg	55.0	55.0
R_{int}	0.0182	0.0181
GOF	1.157	1.027
$R(F)^a$	0.0492	0.0195
$R_w(F_o^2)^b$	0.1165	0.0476
Flack parameter	0.119(5)	0.391(17)
Largest diff. peak/hole (e Å^{-3})	0.680/−0.652	1.216/−1.601

$^aR(F) = \sum||F_o| - |F_c||/\sum|F_o|$. $^bR_w(F_o^2) = [\sum w(F_o^2 - F_c^2)^2/\sum w(F_o^2)^2]^{1/2}$.

Powder X-ray diffraction. Powder X-ray diffraction (PXRD) measurements on $KMgCO_3F$ and $Cs_9Mg_6(CO_3)_8F_5$ were performed using a PANalytical X'Pert PRO diffractometer equipped with Cu Kα radiation. Data were collected in the 2θ range of 5°−70° with a step size of 0.008° and a scan time of 0.3 s. No impurities were observed, and the experimental and calculated PXRDs are in very good agreement (Figure S1).

Second-harmonic generation (SHG). Powder SHG measurements were performed on a modified Kurtz-nonlinear optical (NLO) system using a pulsed Nd:YAG Quantel Ultra laser with a wavelength of 1064 and 532 nm. A detailed description of the methodology has been published.[56] As the powder SHG efficiency has been shown to strongly depend on particle size,[57] $KMgCO_3F$ and $Cs_9Mg_6(CO_3)_8F_5$ were ground and sieved into distinct particle size ranges (<20, 20−45, 45−63, 63−75, 75−90, >90 μm). Relevant comparisons with known SHG materials were made by grinding and sieving crystalline α-SiO_2, $LiNbO_3$, and β-BBO into the same particle size ranges. No index matching fluid was used in any of the experiments (Figure 4).

Infrared (IR) spectroscopy. The Fourier transform infrared spectroscopy (FTIR) spectra for $KMgCO_3F$ and $Cs_9Mg_6(CO_3)_8F_5$

DOI: 10.1021/jacs.6b11965
J. Am. Chem. Soc. 2017, 139, 1285−1295

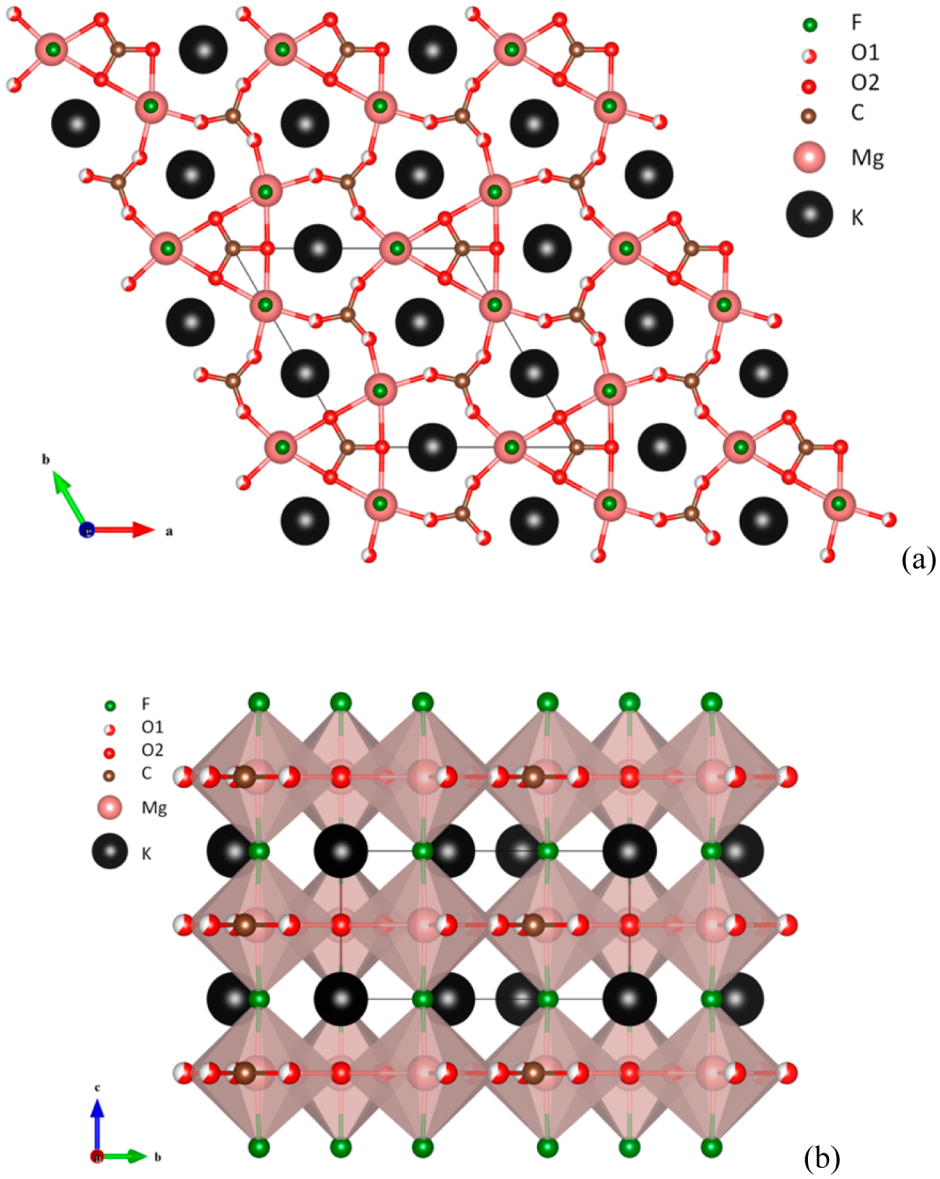

Figure 1. (a) Ball-and-stick representation of $KMgCO_3F$ in the *ab*-plane and (b) polyhedral representation in the *bc*-plane. For clarity, only one position of the disordered $[CO_3]^{2-}$ is shown.

were collected in reflectance mode using a Thermo Scientific Nicolet iS 10 FTIR spectrometer (spectral resolution 4 cm^{-1}) in the range 4000−400 cm^{-1} (Figure S2).

UV−vis diffuse reflectance spectroscopy. UV−visible reflectance data of $KMgCO_3F$ and $Cs_9Mg_6(CO_3)_8F_5$ were collected on a Cary 5000 UV−vis-NIR spectrophotometer over the 200−2000 nm spectral range for diffuse reflectance (Figure 5) at room temperature. Poly(tetrafluoroethylene) was used as a diffuse reflectance standard. The reflectance spectrum of $Cs_9Mg_6(CO_3)_8F_5$ was converted to absorption using the Kubelka−Munk function (Figure S3).[58,59]

Thermal analysis. Thermogravimetric analyses were performed on an EXSTAR TG/DTA 6300 instrument. Approximately 15 mg of $KMgCO_3F$ and $Cs_9Mg_6(CO_3)_8F_5$ were placed separately in a platinum pan and heated at a rate of 10 °C min^{-1} from room temperature to 900 °C under flowing N_2 (Figure S4).

Electronic structure calculations. Structural relaxation and density of states calculations were performed using density functional theory[60] as implemented in the Vienna *ab initio* Simulation Package (VASP).[61,62] The projector-augmented wave (PAW) pseudopotentials[63] and the PBEsol functional were used.[64] The crystal structures of $KMgCO_3F$ and $Cs_9Mg_6(CO_3)_8F_5$ were fixed to the experimental lattice parameters, and the internal atomic positions were relaxed using a 650 eV plane wave cutoff until the forces were less than 0.1 meV/Å. A 6 × 6 × 14 and 2 × 4 × 1 Γ-centered *k*-point mesh was used for $KMgCO_3F$ and $Cs_9Mg_6(CO_3)_8F_5$, respectively. A full structural relaxation was also performed for $CsMgCO_3F$, including the lattice parameters, cell volume, and internal atomic positions using a 650 eV plane wave cutoff and a 6 × 6 × 14 Γ-centered *k*-point mesh. The density of states (DOS) was computed using a 6 × 6 × 14 and an increased 4 × 6 × 2 Γ-centered k-point mesh for $KMgCO_3F$ and $Cs_9Mg_6(CO_3)_8F_5$, respectively. The nonlinear optical coefficients for $KMgCO_3F$ were computing using density functional perturbation theory as implemented in ABINIT[65] using a 650 eV plane wave cutoff and a 5 × 5 × 5 *k*-point mesh. Norm-conserving pseudopotentials were generated using the Troullier−Martins scheme.[66]

RESULTS

Structures. $KMgCO_3F$ crystallizes in the *achiral nonpolar* space group $P\bar{6}2m$ and exhibits a three-dimensional crystal structure consisting of corner-shared $Mg(CO_3)_3F_2$ polyhedra (Figure 1). In $KMgCO_3F$, the Mg^{2+} cations are connected to

DOI: 10.1021/jacs.6b11965
J. Am. Chem. Soc. 2017, 139, 1285−1295

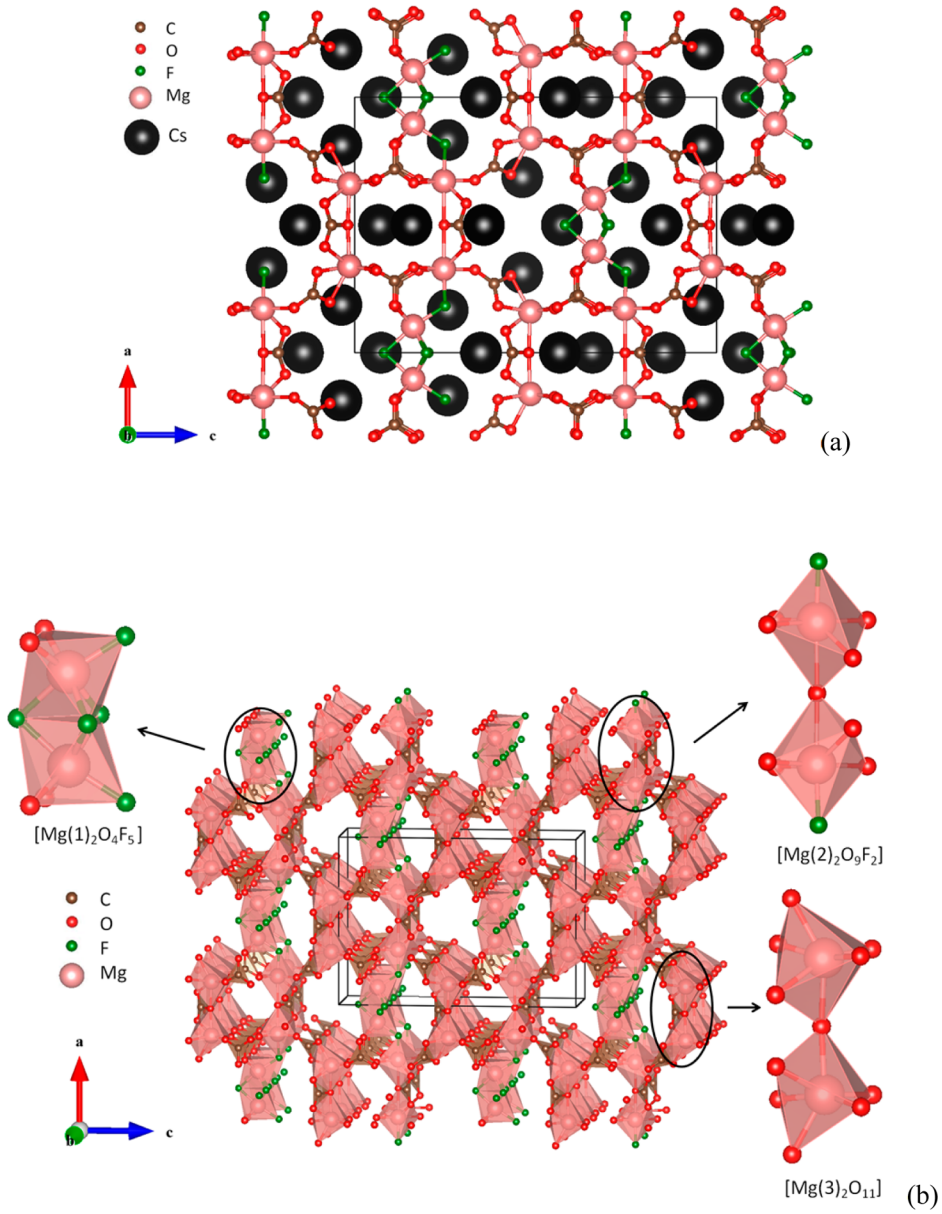

Figure 2. Representations of $Cs_9Mg_6(CO_3)_8F_5$ in the (a) *ac*-plane and (b) *bc*-plane. The Cs cations have been left out for clarity in (b).

three carbonate groups, i.e., two $[C(1)O(1)_3]^{2-}$ units and one $[C(2)O(2)_3]^{2-}$ in the *ab*-plane, and a bridging fluoride along the *c*-direction (Figure 1). The K^+ cations are located in the cavities formed between the $Mg(CO_3)_3F_2$ groups. Two $[C(1)O(1)_3]^{2-}$ groups are observed to be statistically disordered in two orientations with a population of 60%:40%. In connectivity terms, the material may be described as a $[Mg(CO_3)_{3/3}F_{2/2}]^-$ anion, with charge balance maintained by one K^+ cation. Each Mg^{2+} cation is bonded to four oxygen atoms and two fluorine atoms in a distorted octahedral coordination environment, with Mg−O distances of 1.9926(4)−2.2284(5) Å and a Mg−F distance of 1.9637(5) Å. The carbonate C−O bond distances range from 1.1840(2) to 1.2540(3) Å. The K^+ cation is surrounded by six oxygen atoms and three fluorine atoms, with K−O distances of 2.750(4)−2.769(8) Å and K−F distances of 2.973(4)−3.050(10) Å. Bond valence calculations resulted in values of 1.11, 1.92, and 3.60−4.08 for K^+, Mg^{2+}, and C^{4+} respectively (Table S3).

$Cs_9Mg_6(CO_3)_8F_5$ crystallizes in the *achiral polar* space group $Pmn2_1$ and also exhibits a three-dimensional crystal structure consisting of $Mg(1)(CO_3)_2F_4$, $Mg(2)(CO_3)_4F$, and $Mg(3)(CO_3)_4$ polyhedra (Figure 2). In the $Cs_9Mg_6(CO_3)_8F_5$ structure, the $Mg(1)^{2+}$ and $Mg(2)^{2+}$ cations are connected to carbonate groups and bridging fluorides, while the $Mg(3)^{2+}$ cations are only bonded to carbonate groups. The Cs^+ cations are located in the cavities formed between the $Mg(1)(CO_3)_2F_4$, $Mg(2)(CO_3)_4F$, and $Mg(3)(CO_3)_4$ groups. In connectivity terms, the material may be described as $\{2[Mg(1)(CO_3)_{1/3\times2}F_{4/2}]^{4/3-}2[Mg(2)(CO_3)_{1/2}(CO_3)_{1/3\times3}F_{1/2}]^{3/2-}2[Mg(3)(CO_3)_{1/2}(CO_3)_{2/3}(CO_3)_{1/3\times2}]^{5/3-}\}^{9-}$ anions with charge balance maintained by nine Cs^+ cations. All three of the $Mg(1)^{2+}$, $Mg(2)^{2+}$, and $Mg(3)^{2+}$ cations are found to be in distorted octahedral coordination environments of $Mg(1)O_2F_4$, $Mg(2)O_5F$, and $Mg(3)O_6$ (Figure 3), respectively. Each $Mg(1)^{2+}$ cation is connected to two oxygen atoms and four bridging fluorides with Mg(1)−O distances of 2.047(4)−2.051(4) Å and Mg(1)−F distances of 1.975(4)−2.048(3) Å. Each $Mg(2)^{2+}$

DOI: 10.1021/jacs.6b11965
J. Am. Chem. Soc. 2017, 139, 1285−1295

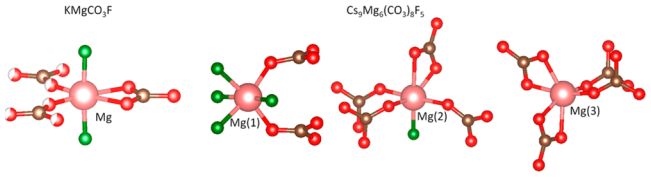

Figure 3. Different coordination denticities for Mg^{2+} cation in $KMgCO_3F$, and for $Mg(1)^{2+}$, $Mg(2)^{2+}$, and $Mg(3)^{2+}$ cations in $Cs_9Mg_6(CO_3)_8F_5$.

cation is connected to five oxygen atoms and a bridging fluoride, with Mg(2)−O distances of 2.033(4)−2.290(2) Å and a Mg(2)−F distance of 1.958(3) Å. Each $Mg(3)^{2+}$ cation is connected to six oxygen atoms, with Mg(3)−O distances of 1.977(4)−2.221(4) Å. The $Cs(1)^+$, $Cs(2)^+$, $Cs(3)^+$, and $Cs(4)^+$ cations are surrounded by oxygen atoms and fluorine atoms in $Cs(1)O_8F$, $Cs(2)O_7F_3$, $Cs(3)O_6F_4$, and $Cs(4)O_5F_4$ polyhedra. The $Cs(5)^+$, $Cs(6)^+$, and $Cs(7)^+$ cations are surrounded by only oxygen atoms in $Cs(5)O_9$, $Cs(6)O_9$, and $Cs(7)O_7$ polyhedra. The Cs−O and Cs−F distances range from 2.944(4) to 3.741(4) Å and from 3.067(3) to 3.447(4) Å, respectively. Bond valence calculations resulted in values of 0.848−1.29, 1.96−2.11, and 3.96−4.05 for Cs^+, Mg^{2+}, and C^{4+}, respectively (Table S3).[67,68]

Second-harmonic generation (SHG) measurements. Powder SHG measurements for $KMgCO_3F$ ($Cs_9Mg_6(CO_3)_8F_5$) using 1064 and 532 nm radiation revealed a SHG efficiency of approximately 120 (20) × α-SiO_2 and 0.33 (0.10) × β-BBO, respectively, in the 45−63 μm particle size range. We further computed the nonlinear optical coefficients of $KMgCO_3F$ using density functional perturbation theory. The third rank NLO tensor of the $-\bar{6}2m$ point group displays three independent components: $d_{11} = -d_{12} = -d_{26}$. For $KMgCO_3F$, we find d_{11} = 0.678 pm/V and $d_{12} = d_{26}$ = −0.678 pm/V. Additional SHG measurements, particle size vs SHG efficiency, indicate the material exhibits type 1 phase-matching behavior (Figure 4). As such, $KMgCO_3F$ and $Cs_9Mg_6(CO_3)_8F_5$ fall into the class A and B categories of SHG materials, respectively, as defined by Kurtz and Perry.[69]

Infrared (IR) spectroscopy. The infrared (IR) spectra of $KMgCO_3F$ and $Cs_9Mg_6(CO_3)_8F_5$ revealed C−O vibrations between 1800 and 680 cm^{-1} (Figure S2). The strong broad bands observed at 1800−1450 cm^{-1} can be assigned to the stretching C−O vibrations. The out-of-plane vibration, δ(OCO), is observed in the range 900−800 cm^{-1}, and the bending vibration, δ(OCO), appears at 700−680 cm^{-1}.[70] The ν(Mg−O) vibration is observed in the range 830−790 cm^{-1}, which can be partially overlapped with δ(OCO).[70] The bands observed at 540−450 cm^{-1} correspond to the ν(Mg−F) stretching vibration.[71]

UV−vis diffuse reflectance spectroscopy. The UV−vis diffuse reflectance spectra indicate that $KMgCO_3F$ and $Cs_9Mg_6(CO_3)_8F_5$ exhibit wide transparency ranges from 2000 to ∼200 nm. The absorption edges for $KMgCO_3F$ and $Cs_9Mg_6(CO_3)_8F_5$ are below 200 nm and at 208 nm,

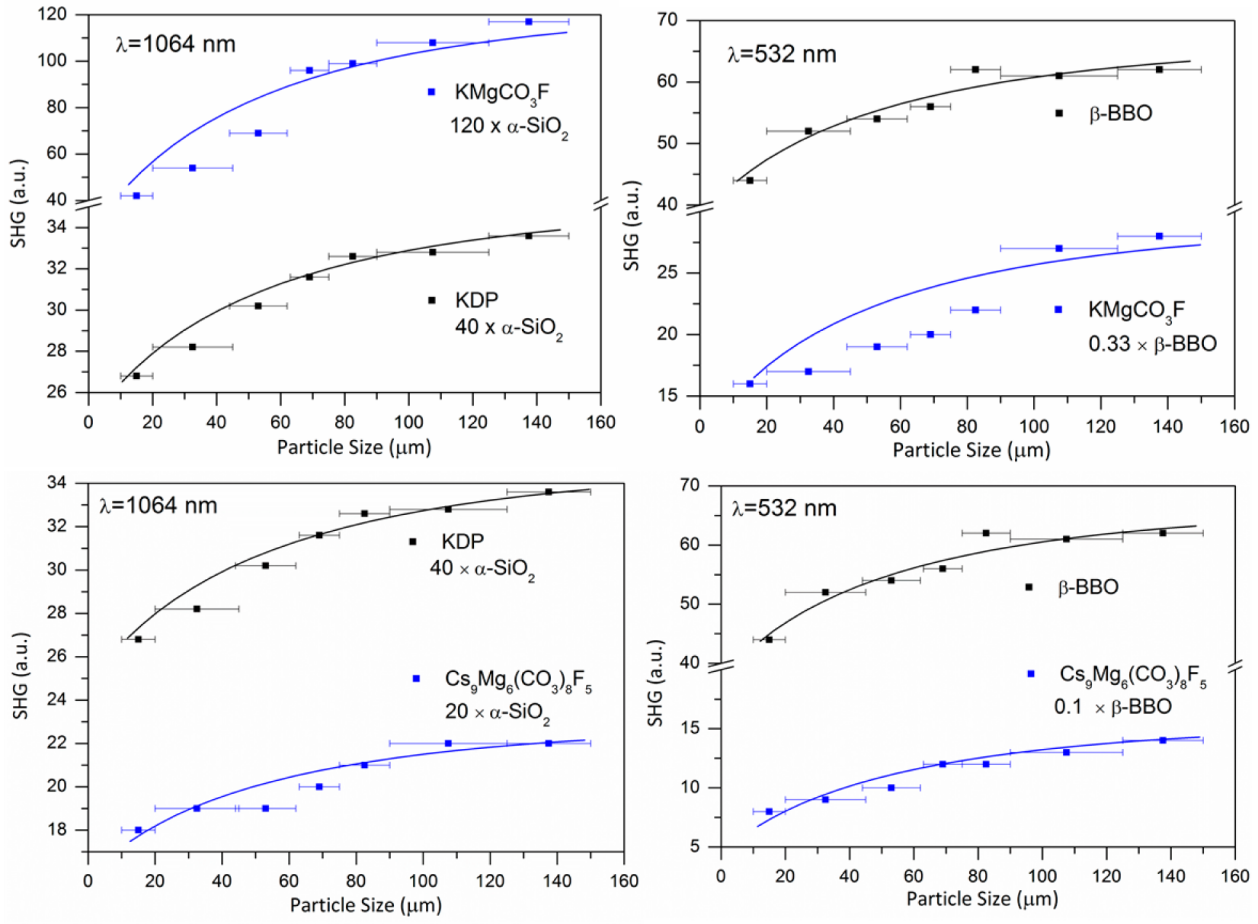

Figure 4. Powder second-harmonic generation at 1064 and 532 nm for $KMgCO_3F$ and $Cs_9Mg_6(CO_3)_8F_5$.

DOI: 10.1021/jacs.6b11965
J. Am. Chem. Soc. 2017, 139, 1285−1295

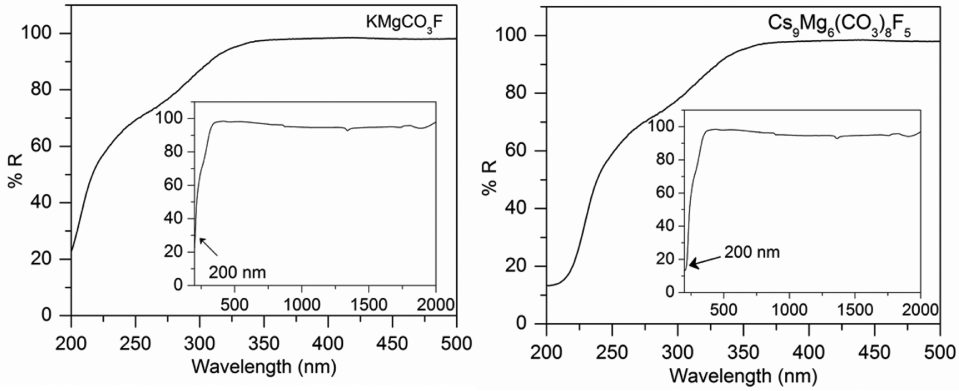

Figure 5. UV−vis diffuse reflectance spectra for $KMgCO_3F$ and $Cs_9Mg_6(CO_3)_8F_5$.

respectively. The UV−vis diffuse reflectance spectra for both materials are shown in Figure 5. In addition, the reflectance spectrum for $Cs_9Mg_6(CO_3)_8F_5$ was calculated using the Kubelka−Munk function.[58,59]

$$F(R) = \frac{(1-R)^2}{2R} = \frac{K}{S}$$

where R represents the reflectance, K the absorption coefficient, and S the scattering factor. In a K/S versus E (eV) plot, extrapolating the linear part of the rising curve to zero resulted in the onset of absorption at 5.96 eV (~208 nm) (Figure S3).

Thermal analysis. The thermal behavior of $KMgCO_3F$ and $Cs_9Mg_6(CO_3)_8F_5$ was investigated using thermogravimetric analysis (TGA) and differential thermal analysis (DTA) under N_2 atmosphere. The decomposition of $KMgCO_3F$ and $Cs_9Mg_6(CO_3)_8F_5$ begins at approximately 390 and 375 °C, respectively, corresponding to the loss of CO_2. The experimental weight loss is in good agreement with the calculated weight loss. The endothermic peaks in the heating curve are consistent with the decomposition of the materials. At approximately 600 and 725 °C, the reduction in mass was observed in the TGA plots that are likely attributable to the loss of fluorides for $KMgCO_3F$ and $Cs_9Mg_6(CO_3)_8F_5$. The exothermic peaks in the cooling cycle indicate recrystallization of the residues occurred at approximately 830 and 775 °C for $KMgCO_3F$. This is confirmed by the appearance of MgO (for both $KMgCO_3F$ and $Cs_9Mg_6(CO_3)_8F_5$) and KF in the powder XRD pattern of the residuals (for $KMgCO_3F$). The DTA/TGA diagrams and powder XRD spectra for $KMgCO_3F$ and $Cs_9Mg_6(CO_3)_8F_5$ are available in the Supporting Information (Figures S4 and S5).

Electronic structure. First-principles density functional theory (DFT) calculations were performed to better understand the stability and linear and nonlinear optical properties. In our previous work[51] we predicted that $CsMgCO_3F$ would have a greater SHG efficiency compared with $RbMgCO_3F$; however, $CsMgCO_3F$ was not found as a product in any of our syntheses. To understand this discrepancy, we computed the enthalpy of formation of $Cs_9Mg_6(CO_3)_8F_5$ and that of the hypothetical $CsMgCO_3F$ compound. In agreement with the experimental results, we found $Cs_9Mg_6(CO_3)_8F_5$ to have a greater thermodynamic driving force by 130 kJ/mol, which we attribute in part to the extremely large cation variance (0.28) with Cs and Mg in the carbonate-fluoride $CsMgCO_3F$. The cation variance gives a measure of the size difference between the atomic species occupying the A- and B-sites, with a larger value indicating a larger difference; the cation variance of n species, each with radius r_n, is given by the formula $\frac{1}{2}\sum_n \frac{(r_n - r_{avg})^2}{(n-1)}$, where r_{avg} is the average radius of the two cations. The variance is greater than any of the isostructural carbonate fluorides such as $KMgCO_3F$ (0.17), $RbMgCO_3F$ (0.21), or those reported in ref 51, which destabilizes the achiral nonpolar $P\bar{6}2m$ $AMCO_3F$ structure-type.

$KMgCO_3F$ and $Cs_9Mg_6(CO_3)_8F_5$ exhibit different coordination denticities of the Mg^{2+} cations (Figure 3). To investigate these differences on the electron charge distribution, we computed the electron localization function (ELF), Figure S6. As with other carbonate fluorides, these materials both exhibit clover-shaped electron densities about the oxide anions comprising the carbonate group. $KMgCO_3F$, similar to previously discovered $RbMgCO_3F$,[51] contains only Mg^{2+} cations exhibiting one bidentate linkage and two monodentate linkages with the oxide anions: The carbonate groups contain either only bidentate oxide anions, i.e., each connected to two Mg cations, or all monodentate oxide anions (see Figure S7). These two environments display qualitatively different electron densities, with those surrounding the monodentate oxygen atoms being more "puckered". In contrast, $Cs_9Mg_6(CO_3)_8F_5$ exhibits three distinct Mg^{2+} bonding environments: one with two bidentate and three monodentate linkages, one with two monodentate linkages (Figure S6b), and one with one bidentate and three monodentate linkages to oxide anions. The carbonate groups of this material either display one bidentate and two monodentate oxygen configurations (Figure S7b) or three monodentate configurations (Figures S6c and S6d). Unlike $KMgCO_3F$, however, there is no discernible difference in the shape of the electron density around any of the oxide anions. Previous work on $RbM^{2+}CO_3F$ ($M = Mg^{2+}$, Ca^{2+}, Sr^{2+}) compounds has shown that as the degree of denticity of the anionic CO_3^{2-} groups increases, the magnitude of the SHG response increases as well.[51] This, along with the fact that the carbonate groups in $KMgCO_3F$ are cooperatively aligned and lie in the same plane, whereas those in $Cs_9Mg_6(CO_3)_8F_5$ do not, give rise to the large discrepancy in the NLO properties.

We also computed the atom-resolved density of states for $KMgCO_3F$ (Figure 6a) and $Cs_9Mg_6(CO_3)_8F_5$ (Figure 6b), and obtain band gaps of 4.63 and 4.19 eV, respectively. Although this underestimation of the electronic band gap is a well-known shortcoming of standard exchange-correlation functionals in DFT,[72] the relative magnitude observed experimentally between the compounds is reproduced, with the band gap of $KMgCO_3F$ being larger than that of $Cs_9Mg_6(CO_3)_8F_5$. Because

DOI: 10.1021/jacs.6b11965
J. Am. Chem. Soc. 2017, 139, 1285−1295

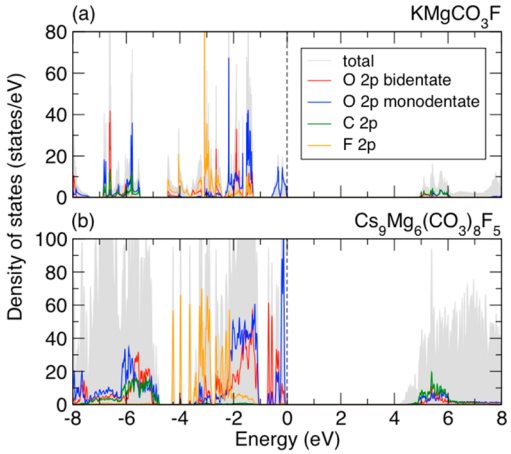

Figure 6. Atomic resolved density of states of (a) $KMgCO_3F$ and (b) $Cs_9Mg_6(CO_3)_8F_5$.

the virtual excitations responsible for second harmonic generation in noncentrosymmetric materials occur between the valence band maximum and conduction band minimum, we next investigate the character of these band edges. In both cases, the top of the valence band consists primarily of oxygen 2p states, which extend to approximately −3 eV and contribute slightly to the bottom of the conduction band. Furthermore, the fluorine 2p states range from −4 to −2 eV, while the carbon 2p states are deeper in the valence band (below −5 eV) and make up the bottom of the conduction band. To understand the aforementioned effect of denticity, we further decomposed the oxygen 2p states into those contributed by bidentate coordinated (red) and monodentate coordinated (blue) anions. All of the states near the top of the valence band in $KMgCO_3F$ consist solely of those from monodentate oxygen ligands, while the bidentate oxygen states only contribute below ∼ −1.5 eV. In contrast, the 2p states from both monodentate and bidentate oxygen atoms overlap strongly from −3 to 0 eV (albeit with slightly more monodentate states near 0 eV).

DISCUSSION

Structures. $KMgCO_3F$ is structurally similar to that of $RbMgCO_3F$.[51] It is, however, observed that $KMgCO_3F$ exhibits disordered oxygen in the $[C(1)O_3]$ group, whereas the $RbMgCO_3F$ structure is completely ordered. The O1 atom in $KMgCO_3F$ was initially refined to be fully occupied on a *m*.. site (x,y,1/2), that created a pentagonal arrangement of $Mg(CO_3)_3$ groups in the *ab*-plane similar to $RbMgCO_3F$.[51] However, the components of the anisotropic displacement in the *ab*-plane, U_{11} and U_{22}, were very large, ∼ 6 and 9 × U_{33}, respectively. The large U_{11} and U_{22} clearly indicated that the O1 atom was partially occupied on the *m*.. site and was displaced by a significant distance, 0.40(2) Å, from this crystallographic site. The disorder results in two orientations of the $[C(1)O_3]$ group in the *ab*-plane with population of 60%$[C(1)O(1)_3]$/40%$[C(1)O(1')_3]$. $[C(1)O(1')_3]$ is rotated about the *c*-axis by 38.4(4)° with respect to $[C(1)O(1)_3]$. The rotational disorder of the CO_3 group has been observed previously in carbonate minerals, such as $CaCO_3$ and $SrCO_3$[73−75] The *x*- and *y*-coordinate parameters of O1 and O1′ were allowed to refine independently, resulting in converged values of 0.179(2) and 0.635(2) for O1, and 0.249(3) and 0.738(3) for O1′, respectively (Figure S7). The thermal displacement parameters of all the atoms in the $KMgCO_3F$ structure were refined anisotropically, excluding O1 and O1′, attributable to their disorder. To ascertain whether the observed disorder with that population is identical to those of different crystals from different batches and what type of disorder (static or dynamic) is more plausible, the disorder was further investigated on a few crystals through single crystal diffraction at low temperature (100 K). No change in the disorder distribution of $[C(1)O(1)_3]$:$[C(1)O(1')_3]$, 60%:40%, was unambiguously observed at 100 K, indicating that the disorder is consistent and likely static.

Further examination of the two related materials, $KMgCO_3F$ and $RbMgCO_3F$,[51] reveals some similarities and differences in the crystallographic architecture. Both materials crystallize in the hexagonal space group $P\bar{6}2m$, with the *c*-axes virtually identical (3.9254(1) vs 3.9403(2) Å for the K and Rb compounds, respectively), as these parameters are defined by the Mg−F bonding distances. The *a* and *b* unit cell parameters, however, are different (8.8437(2) (K) vs 9.0160(3) Å (Rb)), and these are a function of the $Mg(CO_3)_3$ bonding patterns associated with the size of the alkaline cation (see Figure 1). $KMgCO_3F$ and $RbMgCO_3F$ are structurally similar and built up from the $Mg(CO_3)_3F_2$ building units. With respect to the A^+ cations, the effective nine-coordinate ionic radii are 1.55 and 1.63 Å for K^+ and Rb^+, respectively.[76] If we replace K^+ with the larger Rb^+ cation in the structure, we notice that the cavity separation is not very big. In other words, when the larger Rb^+ cation is introduced into the crystal structure, a lattice strain is produced inside the cavities between the $Mg(CO_3)_3F_2$ frameworks. To minimize this strain, the $Mg(CO_3)_3$ layers need to slightly separate in the *ab*-plane to accommodate the larger Rb^+ cation. This phenomenon is clearly observed in the increase of the *a*- and *b*-axes of the unit cell parameters (see Table 1). The *a*- and *b*-axes of $RbMgCO_3F$ are longer than those of $KMgCO_3F$, whereas the *c*-axis remains essentially constant. In addition, the orientational disorder of the $[C(1)O_3]$ group was not observed in $RbMgCO_3F$. The disordered $[C(1)O(1)_3]$:$[C(1)O(1')_3]$ in $KMgCO_3F$ deforms the pentagonal channels of $Mg(CO_3)_3$ in the *ab*-plane.

The crystal structure of $Cs_9Mg_6(CO_3)_8F_5$ features unique $[Mg(1)_2O_4F_5]$, $[Mg(2)_2O_9F_2]$, and $[Mg(3)_2O_{11}]$ dimeric units, connecting through F atoms and/or CO_3 groups (Figure 2). Each $[Mg(1)_2O_4F_5]$, $[Mg(2)_2O_9F_2]$, or $[Mg(3)_2O_{11}]$ dimer is composed of two distorted octahedra, i.e., face-sharing $Mg(1)O_2F_4$, corner-sharing $Mg(2)O_5F$, or corner-sharing $Mg(3)O_6$ octahedra, respectively. Two octahedra in each dimeric unit are symmetry related by the mirror plane perpendicular to the *a*-axis.

Motivated by the occurrence of three entirely dissimilar dimeric units (Figure 3), $Cs_9Mg_6(CO_3)_8F_5$ was further examined considering the stability of microscopic atomic structures. Pauling's five rules have been known as a principle for predicting and rationalizing the crystal structures in ionic compounds, including the radius ratio (I), electrostatic valence (II), polyhedral sharing (III), atomic coordination (IV), and parsimony rule (V).[77] The atomic configurations of the $[Mg(1)_2O_4F_5]$, $[Mg(2)_2O_9F_2]$, and $[Mg(3)_2O_{11}]$ dimeric units present in the $Cs_9Mg_6(CO_3)_8F_5$ crystal structure violate Pauling's third and fifth rules. Pauling's third rule states that corner-shared polyhedra are more favorable than edge-shared ones, which in turn are more stable than face-shared ones, owing to the increased cation−cation electrostatic repulsion.[77] In $Cs_9Mg_6(CO_3)_8F_5$, however, two $Mg(1)O_2F_4$ octahedra sharing a common face of three fluoride atoms are observed.

DOI: 10.1021/jacs.6b11965
J. Am. Chem. Soc. 2017, 139, 1285−1295

Table 2. Summary of $AMCO_3F$ (A = alkali metal, M = alkaline earth metal, Zn, Cd, or Pb) Compounds

Compound	Powder SHG Efficiency	Absorption Edge	Denticity of M-(CO_3)	ref
$CsPbCO_3F$	7.5 (13) × KDP (300 (540) × α-SiO_2)	300 nm (4.15 eV)	3 bidentate	44 (45)
$RbPbCO_3F$	6.25 × KDP (250 × α-SiO_2)	302 nm (4.1 eV)	3 bidentate	45
$KCdCO_3F$	4.58 × KDP (183 × α-SiO_2)	235 nm (5.30 eV)	3 monodentate	50
$KCaCO_3F$	3.61 × KDP (145 × α-SiO_2)	<200 nm (>6.2 eV)	3 bidentate	46
$KSrCO_3F$	3.33 × KDP (130 × α-SiO_2)	<200 nm (>6.2 eV)	3 bidentate	46
$RbSrCO_3F$	3.33 × KDP (130 × α-SiO_2)	<200 nm (>6.2 eV)	3 bidentate	46
$RbMgCO_3F$	4 × KDP (160 × α-SiO_2)	<190 nm (>6.5 eV)	2 monodentate 1 bidentate	51
$KMgCO_3F$	3 × KDP (120 × α-SiO_2)	<200 nm (>6.2 eV)	2 monodentate 1 bidentate	this work
$RbCdCO_3F$	2.8 × KDP (112 × α-SiO_2)	233 nm (5.35 eV)	3 monodentate	50
$KZnCO_3F$	1.76 × KDP (70 × α-SiO_2)	390 nm (3.17 eV)	3 monodentate	50
$CsSrCO_3F$	1.2 × KDP (48 × α-SiO_2)	<200 nm (>6.2 eV)	1 monodentate 2 bidentate	47
$RbCaCO_3F$	1.11 × KDP (45 × α-SiO_2)	<200 nm (>6.2 eV)	1 monodentate 2 bidentate	46
$CsCaCO_3F$	1.11 × KDP (45 × α-SiO_2)	<200 nm (>6.2 eV)	1 monodentate 2 bidentate	46
$RbZnCO_3F$	0.83 × KDP (33 × α-SiO_2)	384 nm (3.23 eV)	3 monodentate	50

Table 3. $AMCO_3F$ SHG Active Materials (A = alkali metal, A′ = alkaline earth, Zn, Cd, or Pb)[a]

	Mg	Ca	Sr	Ba	Zn	Cd	Pb
Li	N.R.	N.R.	N.R.	N.R.	N.R.	N.R.	N.R.
Na	N.R.	N.R.	N.R.	N.R.	N.R.	N.R.	N.R.
K	$KMgCO_3F$ this work	$KCaCO_3F$[46]	$KSrCO_3F$[46]	N.R.	$KZnCO_3F$[50]	$KCdCO_3F$[50]	N.R.
Rb	$RbMgCO_3F$[51]	$RbCaCO_3F$[46]	$RbSrCO_3F$[46]	N.R.	$RbZnCO_3F$[50]	$RbCdCO_3F$[50]	$RbPbCO_3F$[45]
Cs	N.R.[b]	$CsCaCO_3F$[46]	$CsSrCO_3F$[47]	N.R.[c]	N.R.	N.R.	$CsPbCO_3F$[44,45]

[a]N.R. - Not reported [b]$Cs_9Mg_6(CO_3)_8F_5$; this work. [c]$Cs_3Ba_4(CO_3)_3F_5$.[46]

Furthermore, the chemically different coordination environments of three isovalent $Mg(1)^{2+}$, $Mg(2)^{2+}$, and $Mg(3)^{2+}$ cations (Figure 3) also violate Pauling's fifth rule, which states that the number of different kinds of polyhedra in any crystal structure will be small.

For carbonate fluoride materials, the spatial arrangement of the acentric CO_3 groups with respect to the entire structure has been previously described.[78−80] It has been observed that, in carbonate fluorides, the CO_3 group may be oriented in parallel or inclined fashion with regard to the rest of the structure. The CO_3 groups in $KMgCO_3F$ are parallel to the overall structure, similar to other three-dimensional carbonate fluorides, such as $RbMgCO_3F$ and $AMCO_3F$ (A = K, Rb, or Cs; B = Ca or Sr).[51,81] The CO_3 groups in $Cs_9Mg_6(CO_3)_8F_5$ are inclined, similar to $Cs_3Ba_4(CO_3)_3F_5$.[46] In $KMgCO_3F$, the asymmetric coordination environments of the Mg^{2+} atoms are polar; that is, each MgO_6F_2 polyhedron exhibits a local dipole moment. Since the structure is composed of MgO_6F_2 polyhedra with equal polarization magnitudes but aligned in opposite directions, the net dipole moment in the material is zero. Thus, the crystal structure is macroscopically not polar, similar to $RbMgCO_3F$.[51]

In contrast to $Cs_9Mg_6(CO_3)_8F_5$, the polar units of the distorted $Mg(1)O_2F_4$, $Mg(2)O_5F$, and $Mg(3)O_6$ octahedra align in a manner such that the local polarities do not cancel, resulting in macroscopic polarity along the *c*-axis direction.

Recently, there has been a discrepancy in the reported crystal structures of $ACdCO_3F$ (A = K or Rb).[48−50] $KCdCO_3F$ (a = 5.1324(6) Å, c = 4.4324(5) Å;[48] or a = 5.1287(2) Å, c = 4.4277(2) Å[49]) and $RbCdCO_3F$ (a = 5.2101(2) Å, c = 4.5293(2) Å)[49] were observed to crystallize in space group $P\bar{6}m2$ by Mao et al. and Ok et al. However, Ye and co-workers reported $KCdCO_3F$ (a = 5.1349(13) Å, c = 8.846(4) Å) and $RbCdCO_3F$ (a = 5.2109(7) Å, c = 9.0645(19) Å) crystallize in space group $P\bar{6}c2$.[50] Notably, the *c*-axes of $ACdCO_3F$ (A = K or Rb) in Mao's and Ok's publication are half of those reported by Ye et al. By re-examining the crystal structures of these materials, we found that our results are consistent with Ye's. A possible reason for the misleading unit cell determination and structural modeling in $ACdCO_3F$ is the systematically weak *hkl* reflections observed where $l = 2n + 1$. These reflections arise from the special positions of the atoms of $ACdCO_3F$ in space

DOI: 10.1021/jacs.6b11965
J. Am. Chem. Soc. 2017, 139, 1285−1295

group $P\bar{6}c2$; that is, no atoms other than oxygen contribute to the *hkl* reflections where *l* is odd.

Structure−property relationships. In order to better understand the relationships between the NCS structures of the carbonate fluorides and their SHG properties, we plotted the SHG efficiency vs SAMD vs cation variance in a ternary diagram (see Figure 7). In this plot, the SHG efficiency and

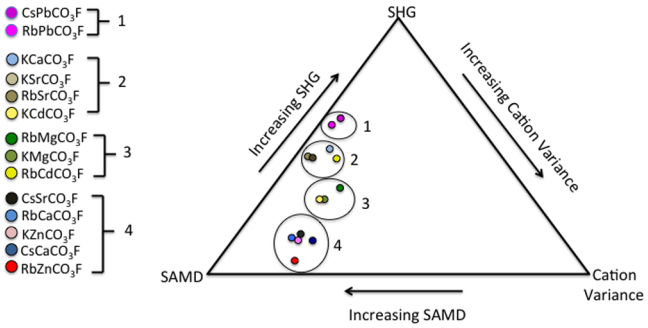

Figure 7. Relationships among SHG efficiency, SAMD, and cation variance in mixed-metal SHG active carbonate fluorides: $AMCO_3F$ (A = alkali metal, M = alkaline earth, Zn, Cd, or Pb).

SAMD have been normalized to be on the same scale as the cation variance. The SAMD (specific acentric mode displacement parameter) enables one to quantify the extent of the acentricity in any NCS structure by comparing it to a hypothetical undistorted structure that does not contain the acentricity.[82] The magnitude of the atomic displacements required to related the two structures is then normalized to the unit cell volume, giving a quantification of acentricity. This simple descriptor can then be used to compare different materials. As shown in Figure 7, the known $AMCO_3F$ materials can be divided into four groups (see also Table 2). The group with the largest SHG efficiency contains $RbPbCO_3F$ and $CsPbCO_3F$. Not surprisingly, the addition of Pb^{2+} with its stereoactive lone-pair increases the SHG efficiency of the carbonate fluoride. However, including Pb^{2+} red-shifts the absorption edge to ∼300 nm (see Table 2). As such, these materials are not useful in the UV or DUV. As we examine groups 2, 3, and 4, we note that the SHG efficiency decreases (on average) with larger A and smaller M cations, or conversely, a greater SHG efficiency is observed for smaller A and larger M cations. It also seems that a smaller SAMD and moderate variance result in a greater SHG efficiency. It should be noted that there are only 14 reported NLO active compounds in the $AMCO_3F$ family (see Table 3), so the trends described herein should be taken as cursory. Nonetheless, it is clear that there is a relationship between the SHG efficiency, SAMD, and cation variance, and the synthesis and characterization of additional compounds will only aid in clarifying this trend. Also, at present, large single crystals have yet to be grown of any of the reported carbonate fluorides. Thus, refractive index, birefringence, and more detailed NLO measurements have not been performed.

CONCLUSIONS

We synthesized two new SHG active carbonate fluoride materials, $KMgCO_3F$ and $Cs_9Mg_6(CO_3)_8F_5$, for NLO applications in the deep-UV region. Our experiments indicate that the materials are SHG active at both 1064 and 532 nm. In addition, both carbonate fluorides exhibit absorption edges below 225 nm, suggesting (D)UV NLO applications. Using density functional theory calculations, we demonstrated the larger NLO response of $KMgCO_3F$ arises from the unique denticity of the polyhedral units and cooperative alignment of anionic carbonate groups, a feature absent in $Cs_9Mg_6(CO_3)_8F_5$. Finally, we drew comparisons between the SHG response, cation variance, and a descriptor of acentricity (specific acentric mode displacement, SAMD) across the $AMCO_3F$ family of known NLO carbonate fluorides that suggest larger SHG efficiencies are observed for smaller A and larger M cations. We hope that this work will motivate efforts toward synthesizing unreported members of this family, allowing for a better understanding of the interplay of these three features and expanding the array of materials for NLO applications.

ASSOCIATED CONTENT

Supporting Information

The Supporting Information is available free of charge on the ACS Publications website at DOI: 10.1021/jacs.6b11965.

Experimental and calculated powder X-ray diffraction patterns, infrared and UV−vis spectra, thermogravimetric and differential thermal analysis diagrams, electron localization function (ELF) and isosurfaces, select bond distances and angles, atomic coordinates, detailed bond valence calculation tables, and mode-polarization vector analyses (PDF)

X-ray crystallographic file in CIF format (CIF)

AUTHOR INFORMATION

Corresponding Authors

*jrondinelli@northwestern.edu

*psh@uh.edu

ORCID

James M. Rondinelli: 0000-0003-0508-2175

P. Shiv Halasyamani: 0000-0003-1787-1040

Present Addresses

§(T.T.T.) Department of Chemistry, Department of Physics and Astronomy, Institute for Quantum Matter, Johns Hopkins University, Baltimore, MD 21218.

∥(J.Y.) Naval Research Laboratory, 4555 Overlook Ave. SW, Washington, DC 20375.

Notes

The authors declare no competing financial interest.

ACKNOWLEDGMENTS

P.S.H. and T.T.T. thank the Welch Foundation (Grant E-1457) and NSF-DMR-1503573 for support. J.Y. and J.M.R. were supported by NSF-DMR-1454688 and a 3M Non-Tenured Faculty Award, respectively. Density functional theory calculations were performed at the Quest high performance computing facility at Northwestern University, which is jointly supported by the Office of the Provost, the Office for Research, and Northwestern University Information Technology, and the CARBON cluster at the Center for Nanoscale Materials at Argonne National Laboratory, supported by the U.S. DOE, Office of Science, Office of Basic Energy Sciences, under Contract No. DE-AC02-06CH11357.

REFERENCES

(1) Savage, N. *Nat. Photonics* **2007**, *1*, 83.
(2) Cyranoski, D. *Nature* **2009**, *457*, 953.

DOI: 10.1021/jacs.6b11965
J. Am. Chem. Soc. 2017, 139, 1285−1295

(3) Yao, W.; He, R.; Wang, X.; Lin, Z.; Chen, C. *Adv. Opt. Mater.* **2014**, *2*, 411.
(4) Tran, T. T.; Yu, H.; Rondinelli, J. M.; Poeppelmeier, K. R.; Halasyamani, P. S. *Chem. Mater.* **2016**, *28*, 5238.
(5) Xu, K.; Loiseau, P.; Aka, G. *J. Cryst. Growth* **2009**, *311*, 2508.
(6) Yang, Y.; Pan, S.; Hou, X.; Wang, C.; Poeppelmeier, K. R.; Chen, Z.; Wu, H.; Zhou, Z. *J. Mater. Chem.* **2011**, *21*, 2890.
(7) Wu, H.; Pan, S.; Poeppelmeier, K. R.; Li, H.; Jia, D.; Chen, Z.; Fan, X.; Yang, Y.; Rondinelli, J. M.; Luo, H. *J. Am. Chem. Soc.* **2011**, *133*, 7786.
(8) Zhang, M.; Pan, S.; Yang, Z.; Wang, Y.; Su, X.; Yang, Y.; Huang, Z.; Han, S.; Poeppelmeier, K. R. *J. Mater. Chem. C* **2013**, *1*, 4740.
(9) Wu, H.; Yu, H.; Pan, S.; Huang, Z.; Yang, X.; Su, K.; Poeppelmeier, K. R. *Angew. Chem., Int. Ed.* **2013**, *52*, 3406.
(10) Wu, H.; Yu, H.; Yang, Z.; Hou, X.; Su, X.; Pan, S.; Poeppelmeier, K. R.; Rondinelli, J. M. *J. Am. Chem. Soc.* **2013**, *135*, 4215.
(11) Yu, H.; Wu, W.; Pan, S.; Yang, Z.; Hou, X.; Su, X.; Jing, Q.; Poeppelmeier, K. R.; Rondinelli, J. M. *J. Am. Chem. Soc.* **2014**, *136*, 1264.
(12) Yan, X.; Luo, S.; Yao, J.; He, R.; Yue, Y.; Chen, C.; Lin, Z. *Inorg. Chem.* **2014**, *53*, 1952.
(13) Zhao, S.; Gong, P.; Bai, L.; Xu, X.; Zhang, S.; Sun, Z.; Lin, Z.; Hong, M.; Chen, C.; Luo, J. *Nat. Commun.* **2014**, *5*, 1.
(14) Yu, H.; Wu, H.; Pan, S.; Yang, Z.; Hou, X.; Su, X.; Jing, Q.; Poeppelmeier, K. R.; Rondinelli, J. M. *J. Am. Chem. Soc.* **2014**, *136*, 1264.
(15) Chen, C. T.; Wang, G. I.; Wang, X. Y.; Xu, Z. Y. *Appl. Phys. B: Lasers Opt.* **2009**, *97*, 9.
(16) Ye, N.; Tang, D. Y. *J. Cryst. Growth* **2006**, *293*, 233.
(17) McMillen, C. D.; Kolis, J. W. *J. Cryst. Growth* **2008**, *310*, 2033.
(18) Chen, C. T.; Wu, Y. C.; Jiang, A. D.; Wu, B. C.; You, G. M.; Li, R. K.; Lin, S. J. *J. Opt. Soc. Am. B* **1989**, *6*, 616.
(19) Wu, Y. C.; Sasaki, T.; Nakai, N.; Yokotani, A.; Tang, H. G.; Chen, C. T. *Appl. Phys. Lett.* **1993**, *62*, 2614.
(20) Chen, C.; Sasaki, T.; Li, R. K.; Wu, Y.; Lin, Z.; Mori, Y.; Hu, Z.; Wang, J.; Uda, S.; Yoshimura, M.; Kaneda, Y. *Nonlinear Optical Borate Crystals*; Wiley-VCH: Weinheim, Germany, 2012.
(21) Eimerl, D.; Davis, L.; Velsko, S.; Graham, E. K. *J. Appl. Phys.* **1987**, *62*, 1968.
(22) Chung, I.; Kanatzidis, M. G. *Chem. Mater.* **2014**, *26*, 849.
(23) Brant, J. A.; Clark, D. J.; Kim, Y. S.; Jang, J. I.; Zhang, J.-H.; Aitken, J. A. *Chem. Mater.* **2014**, *26*, 3045.
(24) Rosmus, K. A.; Brant, J. A.; Wisneski, S. D.; Clark, D. J.; Kim, Y. S.; Jang, J. I.; Brunetta, C. D.; Zhang, J.-H.; Srnec, M. N.; Aitken, J. A. *Inorg. Chem.* **2014**, *53*, 7809.
(25) Halasyamani, P. S.; Poeppelmeier, K. R. *Chem. Mater.* **1998**, *10*, 2753.
(26) Ra, H.-S.; Ok, K. M.; Halasyamani, P. S. *J. Am. Chem. Soc.* **2003**, *125*, 7764.
(27) Sun, C.-F.; Hu, C.-L.; Xu, X.; Ling, J.-B.; Hu, T.; Kong, F.; Long, X.-F.; Mao, J.-G. *J. Am. Chem. Soc.* **2009**, *131*, 9486.
(28) Donakowski, M. D.; Gautier, R.; Yeon, J.; Moore, D. T.; Nino, J. C.; Halasyamani, P. S.; Poeppelmeier, K. R. *J. Am. Chem. Soc.* **2012**, *134*, 7679.
(29) Yu, H.; Wu, H.; Jing, Q.; Yang, Z.; Halasyamani, P. S.; Pan, S. *Chem. Mater.* **2015**, *27*, 4779.
(30) Yang, B. P.; Hu, C.-L.; Xu, X.; Sun, C.-F.; Zhang, J.-H.; Mao, J.-G. *Chem. Mater.* **2010**, *22*, 1545.
(31) Nguyen, S. D.; Yeon, J.; Kim, S.-H.; Halasyamani, P. S. *J. Am. Chem. Soc.* **2011**, *133*, 12422.
(32) Cao, X.-L.; Hu, C.-L.; Xu, X.; Kong, F.; Mao, J.-G. *Chem. Commun.* **2013**, *49*, 9965.
(33) Yang, B.-P.; Hu, C.-L.; Xu, X.; Huang, C.; Mao, J.-G. *Inorg. Chem.* **2013**, *52*, 5378.
(34) Xu, X.; Yang, B.-P.; Huang, C.; Mao, J.-G. *Inorg. Chem.* **2014**, *53*, 1756.
(35) Jo, H.; Kim, Y. H.; Lee, D. W.; Ok, K. M. *Dalton Trans.* **2014**, *43*, 11752.
(36) Kim, Y. H.; Lee, D. W.; Ok, K. M. *Inorg. Chem.* **2014**, *53*, 1250.
(37) Kang, L.; Luo, S.; Huang, H.; Ye, N.; Lin, Z.; Qin, J.; Chen, C. *J. Phys. Chem. C* **2013**, *117*, 25684.
(38) Grice, J. D.; Maisonneuve, V.; Leblanc, M. *Chem. Rev.* **2007**, *107*, 114.
(39) Chen, C. T.; Yu, W. C.; Lin, R. K. *Chin. Phys. Lett.* **1985**, *2*, 389.
(40) Chen, C. T. *Materials for Nonlinear Optics* **1991**, *455*, 360.
(41) Chen, C. T. *Laser Science and Technology, An international handbook*; 1993; Vol. *15*.
(42) Luo, M.; Ye, N.; Zou, G.; Lin, C.; Cheng, W. *Chem. Mater.* **2013**, *25*, 3147.
(43) Tran, T. T.; Halasyamani, P. S. *Inorg. Chem.* **2013**, *52*, 2466.
(44) Zou, G.; Huang, L.; Ye, N.; Lin, C.; Cheng, W.; Huang, H. *J. Am. Chem. Soc.* **2013**, *135*, 18560.
(45) Tran, T. T.; Halasyamani, P. S.; Rondinelli, J. M. *Inorg. Chem.* **2014**, *53*, 6241.
(46) Zou, G.; Ye, N.; Huang, H.; Lin, X. *J. Am. Chem. Soc.* **2011**, *133*, 20001.
(47) Li, Q.; Zou, G.; Lin, C.; Ye, N. *New J. Chem.* **2016**, *40*, 2243.
(48) Lin, Y.; Hu, C.-L.; Mao, J.-G. *Inorg. Chem.* **2015**, *54*, 10407.
(49) Zou, G.; Nam, G.; Kim, H. G.; Jo, H.; You, T.-S.; Ok, K. M. *RSC Adv.* **2015**, *5*, 84754.
(50) Yang, G.; Peng, G.; Ye, N.; wang, J.; Luo, M.; Yan, T.; Zhou, Y. *Chem. Mater.* **2015**, *27*, 7520.
(51) Tran, T. T.; He, J.; Rondinelli, J. M.; Halasyamani, P. S. *J. Am. Chem. Soc.* **2015**, *137*, 10504.
(52) SAINT. In *Siemens Analytical X-ray Systems*, 4.05 ed.; Madison, WI, 1995.
(53) Sheldrick, G. M.: *Program for Solution of Crystal Structures*; University of Gottingen: Germany, 1997.
(54) Sheldrick, G. M.: *Program for Refinement of Crystal Structures*; University of Gottingen: Germany, 1997.
(55) Farrugia, L. J. *J. Appl. Crystallogr.* **1999**, *32*, 837.
(56) Ok, K. M.; Chi, E. O.; Halasyamani, P. S. *Chem. Soc. Rev.* **2006**, *35*, 710.
(57) Kurtz, S. K.; Perry, T. T. *J. Appl. Phys.* **1968**, *39*, 3798.
(58) Kubelka, P.; Munk, F. Z. *Technol. Phys.* **1931**, *12*, 593.
(59) Tauc, J. *Mater. Res. Bull.* **1970**, *5*, 721.
(60) Hohenberg, P.; Kohn, W. *Phys. Rev.* **1964**, *136*, B864.
(61) Kresse, G.; Hafner, J. *Phys. Rev. B: Condens. Matter Mater. Phys.* **1993**, *47*, 558.
(62) Kresse, G.; Furthmüller, J. *Comput. Mater. Sci.* **1996**, *6*, 15.
(63) Blochl, P. E. *Phys. Rev. B: Condens. Matter Mater. Phys.* **1994**, *50*, 17953.
(64) Perdew, J. P.; Ruzsinszky, A.; Csonka, G. I.; Vydrov, O. A.; Scuseria, G. E.; Constantin, L. A.; Zhou, X.; Burke, K. *Phys. Rev. Lett.* **2008**, *100*, 136406/1.
(65) *Comput. Phys. Commun.* **2009**, *180*, 2582.10.1016/j.cpc.2009.07.007
(66) Troullier, N.; Martins, J. L. *Phys. Rev. B: Condens. Matter Mater. Phys.* **1991**, *43*, 1993.
(67) Brown, I. D.; Altermatt, D. *Acta Crystallogr., Sect. B: Struct. Sci.* **1985**, *B41*, 244.
(68) Brown, I. D. *The Chemical Bond in Inorganic Chemistry*; Oxford University Press: New York, 2002; Vol. *12*.
(69) Abrahams, S. C.; Kurtz, S. K.; Jamieson, P. B. *Phys. Rev.* **1968**, *172*, 551.
(70) Huang, C. K.; Kerr, P. F. *Am. Mineral.* **1960**, *45*, 311.
(71) Lesiecki, M. L.; Nibler, J. W. *J. Chem. Phys.* **1976**, *64*, 871.
(72) Baerends, E. J.; Gritsenko, O. V.; van Meer, R. *Phys. Chem. Chem. Phys.* **2013**, *15*, 16408.
(73) Antao, S. M.; Hassan, I.; Mulder, W. H.; Lee, P. L.; Toby, B. H. *Phys. Chem. Miner.* **2009**, *36*, 159.
(74) Reeder, R. J.; Wenk, H. R. *Am. Mineral.* **1983**, *68*, 769.
(75) Carlson, W. D. *Am. Mineral.* **1980**, *65*, 1252.
(76) Shannon, R. D. *Acta Crystallogr., Sect. A: Cryst. Phys., Diffr., Theor. Gen. Crystallogr.* **1976**, *A32*, 751.
(77) Pauling, L. *J. Am. Chem. Soc.* **1929**, *51*, 1010.
(78) Grice, J. D.; Van, V. J.; Gault, R. A. *Can. Mineral.* **1994**, *32*, 405.

DOI: 10.1021/jacs.6b11965
J. Am. Chem. Soc. 2017, 139, 1285−1295

(79) Grice, J. D.; Gault, A.; Van, V. J. *Can. Mineral.* **1997**, *35*, 181.
(80) Grice, J. D.; Chao, G. Y. *Am. Mineral.* **1997**, *82*, 1255.
(81) Zou, G.; Ye, N.; Huang, L.; Lin, X. *J. Am. Chem. Soc.* **2011**, *133*, 20001.
(82) Cammarata, A.; Zhang, W.; Halasyamani, P. S.; Rondinelli, J. M. *Chem. Mater.* **2014**, *26*, 5773.

DOI: 10.1021/jacs.6b11965
J. Am. Chem. Soc. 2017, 139, 1285−1295